Chapter 5

Aluminium doped Lithium-vacant Layered $Li_{1-x}Cr_{1-x}Al_xO_2$: A Potentially Active Electrocatalyst for Oxygen Evolution Reaction

Chapter 5

Aluminium doped Lithium-vacant Layered $Li_{1-x}Cr_{1-x}Al_xO_2$: A Potentially Active Electrocatalyst for Oxygen Evolution Reaction

5.1 Introduction

Electrochemical water splitting is considered the most promising and highly efficient method to produce highly pure hydrogen (a green fuel) on a large scale with zero emissions [1-4]. However, as the paramount half-reaction of water splitting, the oxygen evolution reaction (OER) plays a critical role in the production of hydrogen. The major obstacle for OER is the sluggish reaction kinetics and high overpotentials due to its complex four-electron-transfer process, $4OH^- \rightarrow 2H_2O + 4e^- + O_2$, making it energetically inefficient in all these technologies [5-7]. To date, precious-metal-based oxides (IrO_2 and RuO_2) are thought to be the most active OER catalysts with the lowest overpotentials, but they are not appropriate for large-scale application due to their high cost, scarcity, and poor stability [8, 9]. Therefore, the key interest is the development of highly efficient non-precious transition metal-based OER electrocatalysts [10]. The redox behavior of transition-metal oxides due to their variable oxidation states that are readily involved in redox reactions with adsorbed molecules are identified as active centers for the OER. Tuning the redox potential of metal complexes and metal (hydr-) joxides can lead to greater OER activity, which can be attributed to optimized binding of the reaction intermediates on the surface in rate-limiting steps [11].

Recently, layered hexagonal $LiMO_2$ (M = Ni, Co, Mn, Fe, Cr) and its analogous have drawn great attention as potential OER catalysts due to the interplay of layered crystal structure and mixing of O(2*p*) band in M(3*d*) levels via the tuning of the oxidation state of transition metal ions by manipulating the Li-content in the structure [12-18]. In a previous report, Lu *et al*. stated that the electrochemical de-lithiation of HT-$LiCoO_2$ (high-temperature phase) to

$Li_{0.5}CoO_2$ in a non-aqueous electrolyte, resulted in high OER mass activity [14]. Similarly, the chemical de-lithiation of LT-$LiCoO_2$ (low-temperature phase) with NO_2BF_4 to LT-$Li_{0.5}CoO_2$ led to significant bifunctional catalytic activity (in terms of OER and ORR) by pinning of the $Co^{3+/4+}$:3*d* energy with the top of the O^{2-}: 2*p* band [15]. In the last few years, a series of layered $LiNi_{1-x}M_xO_2$ (M = Mn, Fe, Co, Al) has been identified as a potential OER electrocatalyst [16-18]. A previous study has shown that doping of Al in $LiNiO_2$ can significantly enhance the OER activity of $LiNiO_2$ by tunning the $Ni^{2+/3+}$ redox energy in the lattice [17]. Zhu *et al*. reported that the catalytic activity of $Li_yNi_{1-x}Fe_xO_2$ can be tuned with different Fe doping amounts and Li content in the composition [18]. Very recently, Cr-based materials have attracted significant attention due to their multi-electron transfer reaction during electrochemical cycling to develop electrodes for Li-ion batteries. For example, $Li_{1.2}Cr_{0.4}Mn_{0.4}O_2$ cathode material shows a redox interaction between octahedral Cr^{3+} and tetrahedral Cr^{6+} during electrochemical cycling, exhibiting a discharge capacity of ~150 mAh g^{-1} and indicating a possibility of three-electron transfer [19-20].

In our previous report, we found that the presence of Cr^{6+} ions at Li interstitial sites creates a dumbbell defect in the layered $Li_yCr_{1-x}Fe_xO_2$ ($y \leq 1$, $0 \leq x \leq 0.2$) with different Fe doping that facilitates the formation of Cr-O-OH in alkaline media, and thereby enhancing the OER activity of the catalyst [21]. Similarly, smaller Al^{3+} ion can also be substituted in the layered $LiCrO_2$ structure, both at Cr-ion site as well as Li-ion interstitial site, creating dumbbell defects in the lattice. Due to the inductive effect through the formation of highly covalent Al-O bond, the ionicity of the counterpart Cr-O and Li-O bonds in the layered structure can be enhanced that can result in high mobility of Li^+-ion in the lattice as well as lead to superior mixing of Cr(3*d*) and O(2*p*) level ensuing superior OER activity of the Al-doped catalyst. In layered $LiMO_2$ materials, Al is known to stabilize the structure of the cathode material via strong Al-O covalent bonding due to a significant Al(*s*)-O(*p*) overlap, as well as significant charge transfer

capabilities of Al [22]. Herein, we report a systematic investigation of OER activity of layered $Li_{1-x}Cr_{1-x}Al_xO_2$ (x = 0, 0.17, 0.20, 0.25, 0.33), synthesized via conventional solid-state method. Consolidating Rietveld refinement (XRD) and XPS data, it was found that the substitution of larger chromium ions with more polarizing and smaller Al^{3+} ions can significantly increase the effective charge on Cr ions or enhance the ionicity of Cr-O bond that would lead to lower the electron energy associated with the antibonding states of metal-ligand (e.g., oxygen) and shift the redox potential positively. This is accompanied by the shifting of electron density from parent metal to ligand through inductive effect of more polarizing Al^{3+} ions in the lattice. Positive shifting of the redox potential results in the greater overlap between Cr(3*d*) and O(2*p*) orbital leads to higher catalytic activity [11]. In our findings, we believe that the anisotropic behavior of layered lattice coupled with the tuning of ionicity of M-O bonding in layered oxides can be used as an activity descriptor in developing superior OER catalysts.

5.2 Experimental section

5.2.1 Materials synthesis

The solid solution of $Li_{1-x}Cr_{1-x}Al_xO_2$ (x = 0, 0.17, 0.20, 0.25, 0.33) was synthesized by using a conventional solid-state ceramic synthesis method. Stoichiometric amounts of Li_2CO_3 (Sigma Aldrich, ≥ 99 %), Cr_2O_3 (Sigma Aldrich, ≥ 98 %), and Al_2O_3 (Sigma Aldrich, ≥ 98 %) were ground for half an hour in an agate-mortar pestle and first fired at 550 ℃ for 6 h. The intermediate mixture was further reground and then calcined at 800 ℃ for 30 h in an oxygen atmosphere. The samples were denoted as LCAO-0, LCAO-17, LCAO-20, LCAO-25, and LCAO-33 for $LiCrO_2$, $Li_{0.83}Cr_{0.83}Al_{0.17}O_2$, $Li_{0.80}Cr_{0.80}Al_{0.20}O_2$, $Li_{0.75}Cr_{0.75}Al_{0.25}O_2$, $Li_{0.67}Cr_{0.67}Al_{0.33}O_2$ respectively. For electrochemical activity comparisons, samples of α-MnO_2 [23], $Ba_{0.5}Sr_{0.5}Co_{0.8}Fe_{0.2}O_{3-\delta}$ (BSCF) [24], and $LaNiO_3$ [25], were synthesized by following procedures described elsewhere; and a commercial RuO_2 (99 %) was obtained from Sigma-Aldrich and used as received.

5.3 Results and Discussion

5.3.1 XRD studies and Rietveld refinement

Figure 5.1 displays the XRD pattern of LCAO samples ($Li_{1-x}Cr_{1-x}Al_xO_2$; $x = 0$, 0.17, 0.20, 0.25, 0.33) synthesized by solid-state reaction. As can be seen in **Figure 5.1**, all the samples have a characteristic hexagonal α-$NaFeO_2$-type structure with the *R-3m* space group, and all diffraction lines are well-indexed with the standard rhombohedral phase of $LiCrO_2$ (JCPDS No. 00-024-0600). The good separations of the (006)/(012) and the (108)/(110) pairs of diffraction lines indicate the well-ordered layered structure for all the samples [26]. Small additional peaks corresponding to the $LiAl_5O_8$ were observed for LCAO-33, indicating that up to 25 % Al substitution does not affect the bulk structure of $LiCrO_2$.

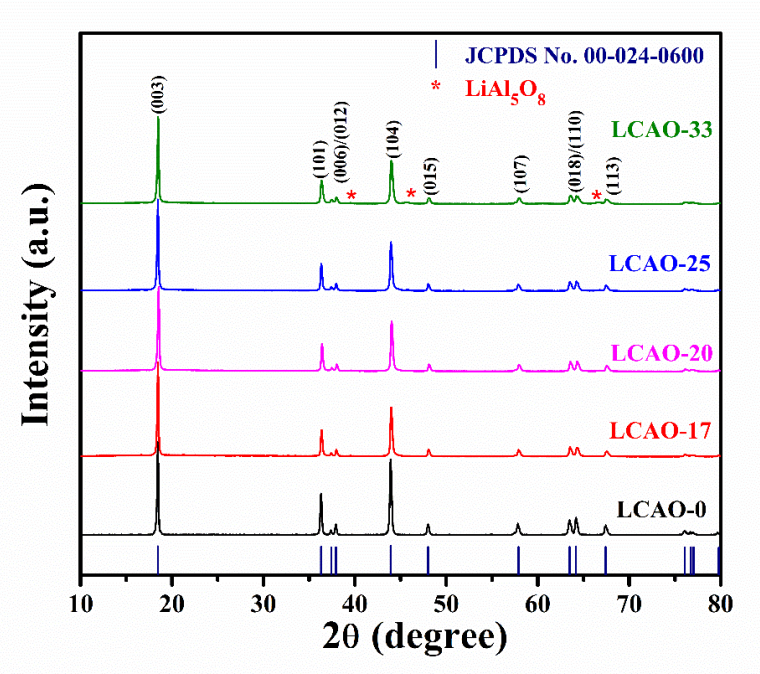

Figure 5.1 XRD pattern of different solid state synthesized LCAO samples.

In addition, the intensity ratios of (003) and (104) peaks, $I_{(003)}/I_{(104)}$, that serve as the indicator of the degree of cation intermixing in the lattice structure [27], have been increased upon substitution of Al in $LiCrO_2$. A higher value of $I_{(003)}/I_{(104)}$ means lower mixing of cations. The

calculated $I_{(003)}/I_{(104)}$ values are 1.29, 1.63, 1.65, 1.69, and 1.70 for LCAO-0, LCAO-17, LCAO-20, LCAO-25, and LCAO-33, respectively. This clearly indicates that Al substitution results in a good ordering of lithium and chromium/aluminium ions in the layered structure. Further, in order to illustrate the effects of Al substitution more efficiently, the Rietveld refinement of XRD patterns was performed using FULLPROF suite software, (see **Figure 5.2**).

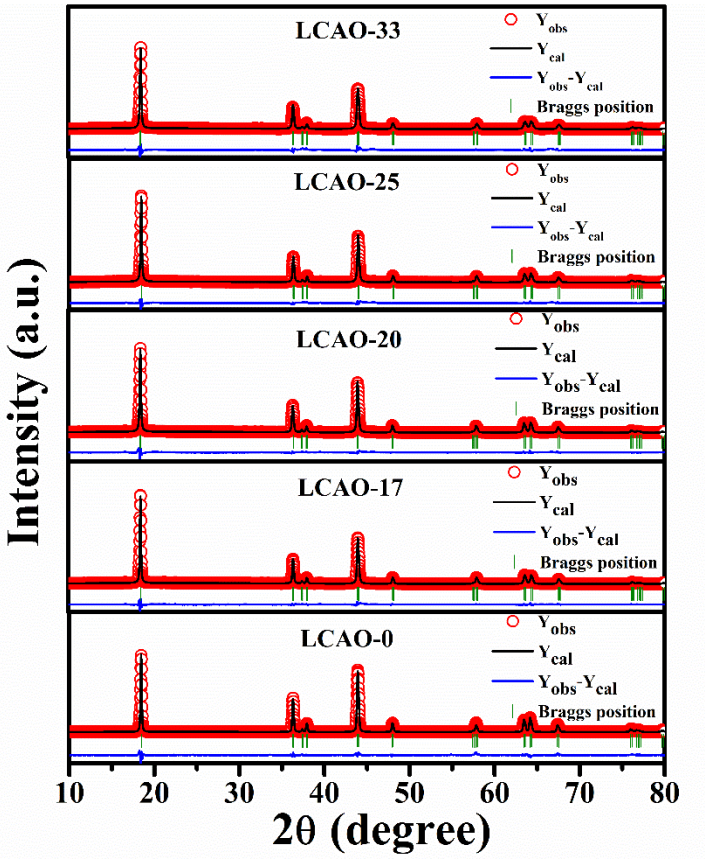

Figure 5.2 Rietveld refined powder XRD patterns of LCAO samples.

In the first step, the structures were refined by taking Pseudo-Voigt as peak profile function and *R-3m* space group (assuming perfectly ordered α-$NaFeO_2$ type structure) in which Cr^{3+}/Al^{3+} ions occupy the 3*a* site (0, 0, 0), Li^+ ions in the 3*b* site (0, 0, 1/2), and O^{2-} ions in the 6*c* site (0, 0, Z_{ox}), (Z_{ox} = 0.24−0.25). Therefore, the site occupancies were fixed, while the isotropic thermal parameters (*B*) were allowed to vary in the refinement process. The calculations led to negative values of the lithium isotropic thermal parameters, *B*(Li), showing an excess of electronic density in the lithium site due to the presence of chromium or aluminium ions in the

interslab space [28]. The refinement results along with their reliability factors (R_{bragg}, R_f, and χ^2) were listed in **Table 5.1**.

Table 5.1 Structural parameters obtained from Rietveld refinement of $Li_{1-x}Cr_{1-x}Al_xO_2$ (x = 0, 0.17, 0.20, 0.25, 0.33) synthesized by solid state reaction method.

Samples	LCAO-0	LCAO-17	LCAO-20	LCAO-25	LCAO-33
a_{hex} (Å)	2.9005(2)	2.8968(4)	2.8966(4)	2.8951(5)	2.8941(5)
c_{hex} (Å)	14.4308(4)	14.4224(2)	14.4201(2)	14.4171(2)	14.4048(7)
c_{hex}/a_{hex}	4.975	4.978	4.978	4.979	4.977
V_{hex} (Å^3)	105.14	104.64	104.79	104.78	104.49
z_{ox}	0.2449(6)	0.2427(5)	0.2421(2)	0.2413(4)	0.2418(7)
$S_{(CrO2)}$ (Å)[a]	2.55(2)	2.61(1)	2.63(1)	2.65(1)	2.64(2)
$I_{(LiO2)}$ (Å)[b]	2.26(2)	2.20(1)	2.18(1)	2.15(1)	2.16(2)
B(Li) Å^2	-0.31(2)	-0.47(2)	-0.92(2)	-1.20(1)	-1.09(3)
χ^2	2.03	2.09	2.11	2.16	2.13
R_{wp}	22.5	13.6	14.3	17.8	21.1
R_{Bragg}	5.5	3.2	3.1	5.6	6.7

Note:

[a] **Slab thickness:** $S_{(MO2)} = 2\,[(1/3 - z_{ox})]\,c_{hex.}$

[b] **Interslab space thickness:** $I_{(LiO2)} = (c_{hex.}/3) - S_{(MO2)}$

According to the refinement results, the hexagonal lattice parameters ($a_{hex.}$ and $c_{hex.}$) decreased linearly with increasing Al concentration in the solid solution. This lattice variation can be explained by using the crystal lattice of α-$LiAlO_2$ (a = 2.800 Å, c = 14.22 Å, *R-3m* [29]) which shows a smaller $a_{hex.}$ and $c_{hex.}$ values than those of $LiCrO_2$. The linear change in lattice parameters by varying the Al concentration in the solid solution is in accordance with Vegard's law [30, 31]. Concerning with $a_{hex.}$ parameter (reflecting the M-M bond length), the idea of the shrinkage is considerably due to the larger chromium ions (Cr^{3+} = 0.615 Å) is replaced with more polarizing and smaller aluminium ions (Al^{3+} = 0.535 Å) [32]. The $c_{hex.}$ lattice parameter is related to the interlayer distance of LiO_2 (interslab space thickness, $I_{(LiO_2)}$) and CrO_2 (slab

thickness, $S_{(CrO_2)}$) layers [28]. As the $c_{hex.}$ parameter decreases, the slab thickness (CrO_2 layer) increases and the interslab space thickness (LiO_2 layer) decreases with increasing the Al concentration in the solid solution due to the formation of strongly covalent Al-O bond. The bonding between the Cr and Al at Li sites and O in the CrO_2 layers shortens the interlayer distance, and the electrostatic attraction between them decreases the total energy of the system. Thus, the Al/Cr antisites finally stabilize the system in Li-deficient sites [33]. **Figure 5.3** represents the crystal structure of $Li_{1-x}Cr_{1-x}Al_xO_2$, which shows a layered rhombohedral structure containing Li-vacancies with the partial mixing of Cr/Al in the Li-layer. The doping of Al can substantially induce the Cr^{6+} ions to be partially occupied at the Li interstitial site creating a dumbbell defect in the hexagonal lattice of $Li_{1-x}Cr_{1-x}Al_xO_2$ and thereby stabilizing the layered structure of the system with partial Li-deficiency and cation mixing.

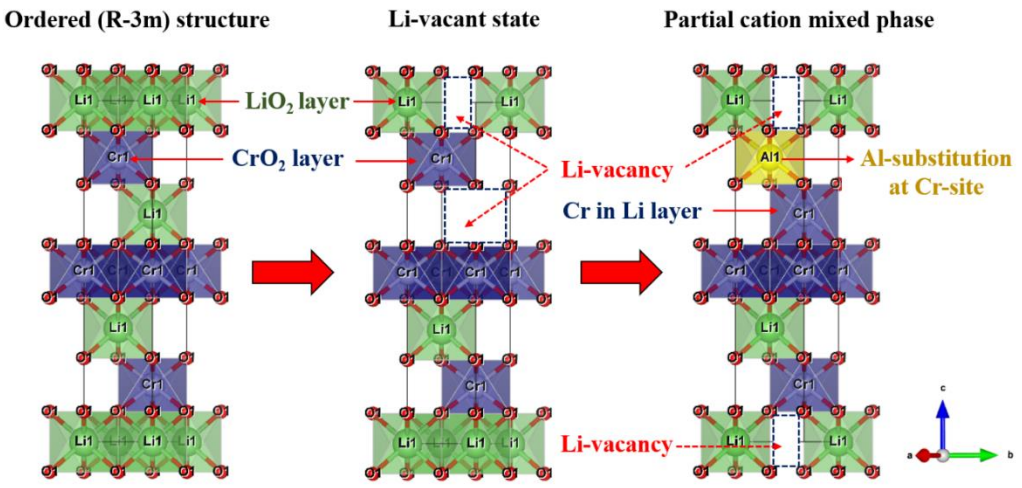

Figure 5.3 Schematic illustration of structural transformation in layered $Li_{1-x}Cr_{1-x}Al_xO_2$.

5.3.2 XPS and ICP analysis:

X-ray photoelectron spectroscopy (XPS) was performed to investigate the electronic structure and valence state of the elements (Li, Cr, Al, and O) present in the material. The high-resolution core level spectra of Cr 2*p* is fitted with two doublet binding energy Cr $2p_{1/2}$ and Cr $2p_{3/2}$, as shown in **Figure 5.4(a, b)** of LCAO-0 and LCAO-25. The de-convoluted peaks exhibit two

chemical states of Cr, (i.e., Cr^{3+} and Cr^{6+}). The $2p_{3/2}$ and $2p_{1/2}$ peaks found at ~575.8 and ~585.7 eV were assigned to Cr^{3+}, and the $2p_{3/2}$ and $2p_{1/2}$ peaks found at ~577.7 and ~587.4 eV were assigned to Cr^{6+} [34, 35] of LCAO-25. The observed ratio between the fractional composition of Cr^{3+} to Cr^{6+} in LCAO-0 is 0.89: 0.11, and in LCAO-25 is 0.72: 0.28. Further, Cr ($2p_{3/2}$) peak shifted around 0.5 eV from 575.3 to 575.8 eV in LCAO-25 from LCAO-0 (no Al-doped sample). This confirms that Al^{3+} substitution in the lattice increases the ionicity of the Cr-O bond in general as well as resulting high concentration of Cr^{6+} ions in the lattice. The more polarizing and smaller Al^{3+} ions can significantly increase the effective charge on Cr ions which would lead to an increase in the ionicity of the Cr-O bond due to the high covalency of the Al-O bond through inductive effect (supported by the refinement results). The Al($2p$) core level spectrum **(Figure 5.4c)** consists of a peak at about 74.5 eV is close to the binding energy of Al^{3+} in $LiAlO_2$ [36]. In addition, a shakeup peak located at about 79.2 eV is also present due to defects present in the lattice [37, 38]. The deconvoluted Li ($1s$) spectra, shown in **Figure 5.4(d, e),** are fitted with two peaks located at ~54.3 and ~55.6 eV that confirm the existence of lithium in two different cation environments (i.e., the octahedral Cr^{3+} polyhedra and the interstitial Cr^{6+} tetrahedra, respectively) in the lattice. Further, the Li 1s peak shifted to a higher binding energy (~0.25 eV) in LCAO-25, confirming the higher ionicity of the Li−O bond in the lattice. The O($1s$) spectra are also fitted with two peaks located at ~529.46 and ~531.27 eV that corroborates the existence of lattice oxygen (O^{2-}) and "non-stoichiometric" surface oxygen or hydroxide (OH^-), respectively, see **Figure 5.4(e, f)** [39].

The relative surface concentrations of Li, Cr, and Al in LCAO-0 and LCAO-25 were calculated by using the formula [40].

$$Relative\ concentration, C_M = \frac{I_M/\lambda_M \sigma_M D_M}{\sum(I_M/\lambda_M \sigma_M D_M)} \quad (5.1)$$

where I_M is the integrated intensity of the core levels (M = Cr $2p$, Al $2p$, and Li $1s$), λ_M is the mean escape depths of the respective photoelectrons, σ_M is the photoionization cross-section,

and D_M is the geometric factor. The photoionization cross-section values were taken from Scofield's data [41] and the mean escape depths were taken from Penn's data [42]. The geometric factor was taken as 1 because the maximum intensity in this spectrometer is obtained at 90º.

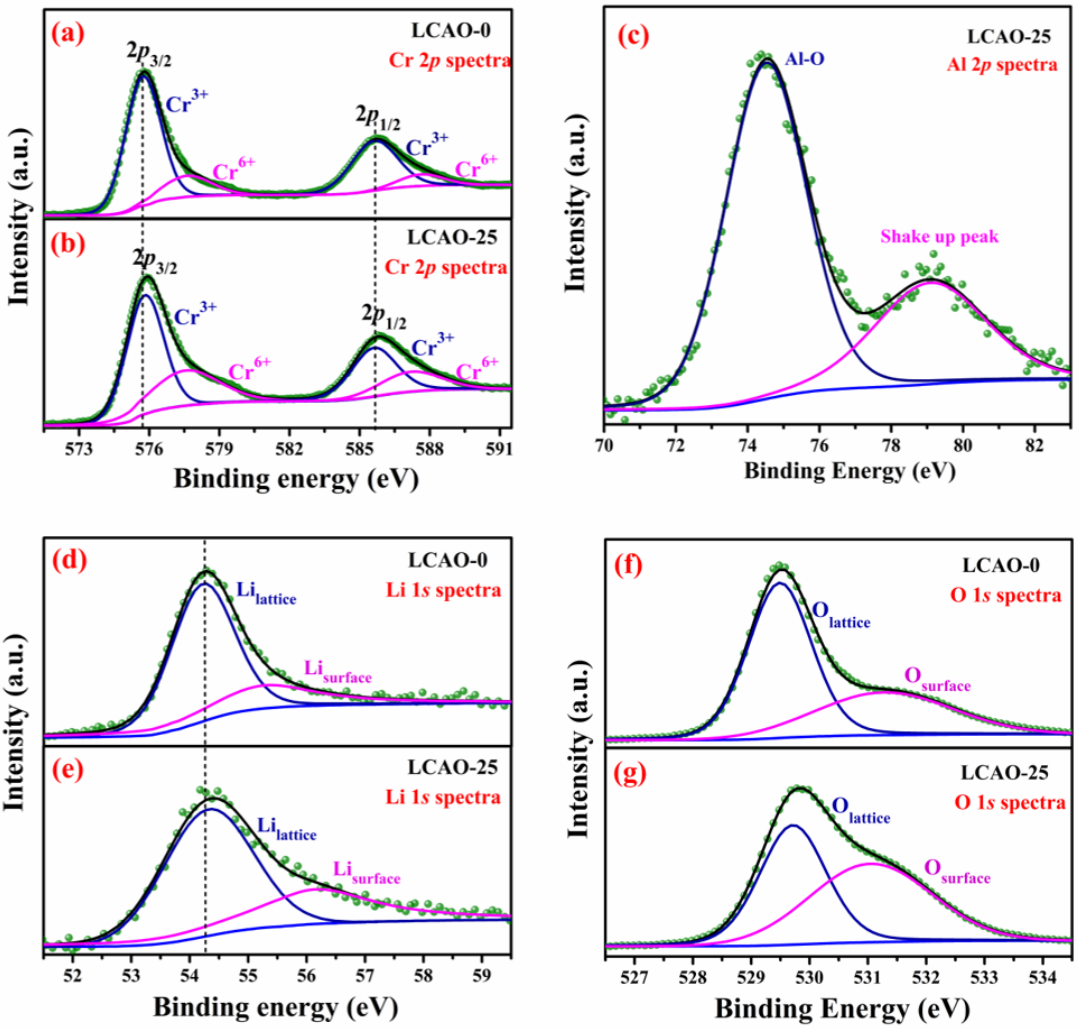

Figure 5.4 Core level XPS spectra of **(a, b)** Cr 2p, **(c)** Al 2p, **(d, e)** Li 1s and **(f, g)** O 1s.

The surface concentrations of Li: Cr: Al were found in the ratio of 0.75: 0.75: 0.25 in $Li_{0.75}Cr_{0.75}Al_{0.25}O_2$, and the Li: Cr ratio was found to be 0.67: 1 in $LiCrO_2$. Further, the relative concentration of Cr, Al, and Li in the samples was also examined by the ICP analysis using Inductively Coupled Plasma Mass Spectrometry (ICP-MS), (make: Agilent 7800 ICP-MS mainframe). The nominal (desired) and actual composition (obtained from the ICP-MS

analysis) of all synthesized $Li_{1-x}Cr_{1-x}AL_xO_2$ (x = 0, 0.17, 0.20, 0.25, 0.33) catalysts are listed in **Table 5.2**. The observed value from the XPS study matches very well with the elemental ratios obtained from the ICP-MS study. Thus, the formula of the compound along with their electronic structure can be represented as $Li_{0.67}Cr^{3+}_{0.89}Cr^{6+}_{0.11}O_2$ and $Li_{0.75}(Cr^{3+}_{0.72}Cr^{6+}_{0.28})_{0.75}Al_{0.25}O_2$ or $Li_{0.75}Cr^{3+}_{0.54}Cr^{6+}_{0.21}Al_{0.25}O_2$, showing high polarization or ionicity of Cr-O bond after Al doping (i.e., Cr^{3+} is getting oxidized to Cr^{6+}), resulting an excess positive charge which is neutralize by non-stoichiometric surface oxygen or OH^- ions.

Table 5.2 Relative concentration of Li, Cr, Al in $Li_{1-x}Cr_{1-x}Al_xO_2$ (x = 0, 0.17, 0.20, 0.25, 0.33) from ICP analysis.

Catalyst	**Nominal Composition**	**ICP composition of $Li_{1-x}Cr_{1-x}Al_xO_2$ (x = 0, 0.17, 0.20, 0.25, 0.33)**		
		Li	**Cr**	**Al**
LCAO-0	**$LiCrO_2$**	0.67	1.00	0.00
LCAO-17	**$Li_{0.83}Cr_{0.83}Al_{0.17}O_2$**	0.83	0.83	0.17
LCAO-20	**$Li_{0.80}Cr_{0.80}Al_{0.20}O_2$**	0.80	0.80	0.20
LCAO-25	**$Li_{0.75}Cr_{0.75}Al_{0.25}O_2$**	0.75	0.75	0.25
LCAO-33	**$Li_{0.67}Cr_{0.67}Al_{0.33}O_2$**	0.67	0.67	0.33

5.3.3 Microstructural studies:

The surface morphology and particle sizes were observed by Scanning electron microscopy (SEM). **Figure 5.5(a, b)** shows the SEM micrograph of LCAO-0 and LCAO-25 synthesized by solid-state reaction. The material shows almost hexagonal morphology, and the particles are non-agglomerated. The particle size decreases with increasing Al-doping amount in the samples. It is clearly seen that LCAO-25 samples **(Figure 5.5b)** possess smaller particles as compared to the LCAO-0 **(Figure 5.5a)**. The particle size distribution is more homogeneous when Al-doping is applied. The elemental analysis of the LCAO-25 sample was carried out by

SEM-EDS technique. The elemental mapping and energy spectrum of the sample are shown in **Figure 5.5(c, d)**. The presence of Cr, Al, and O atoms confirms the successful doping of Al in the sample. The EDS data confirms that the obtained elemental composition (Cr: Al = 0.73: 0.27) in LCAO-25 is almost the same as the nominal composition taken for the synthesis. Since the excitation energy of the Li element is low, therefore, it is not possible to detect the Li in the sample by SEM-EDX.

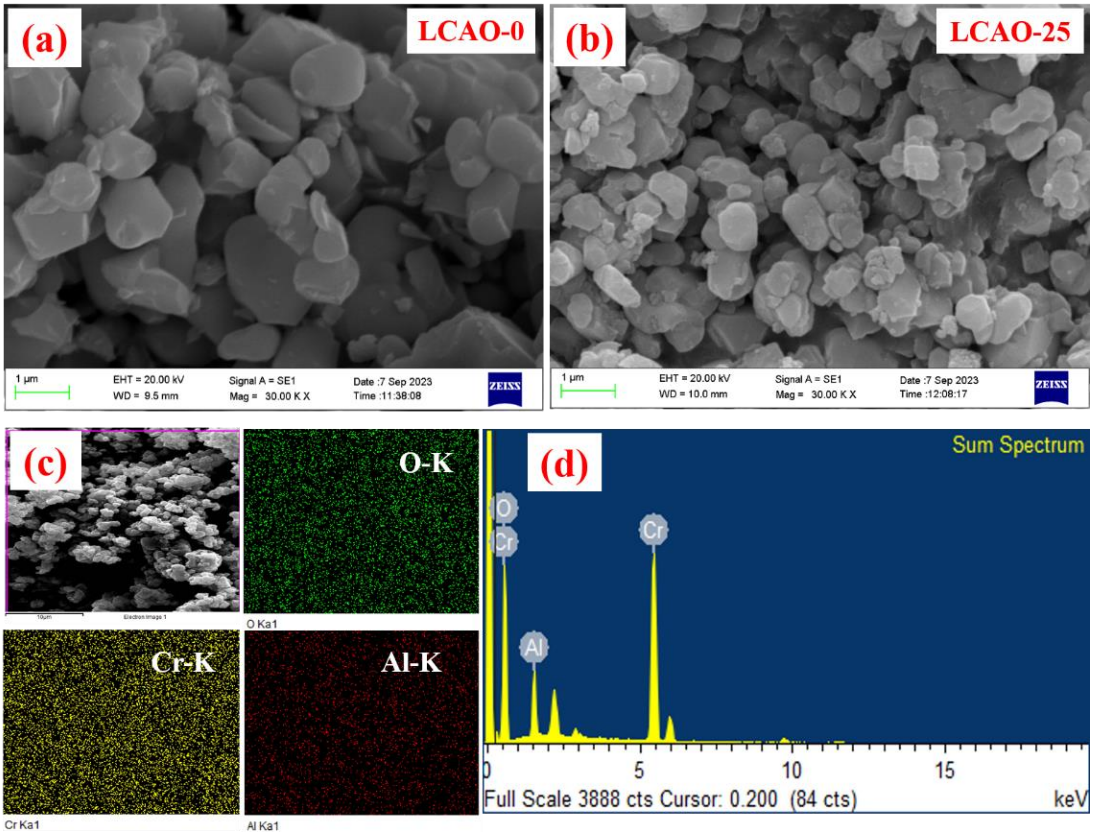

Figure 5.5 SEM micrograph of **(a)** LCAO-0 **(b)** LCAO-25, **(c)** elemental mapping of individual elements (O, Cr, and Al) present in the LCAO-25 sample and **(d)** EDX spectrum of LCAO-25. Note: Li signals are absent in EDX analysis as EDX techniques are not capable of recording signals for the Li core level.

To investigate the phase structure of LCAOs, the HR-TEM and selected area electron diffraction (SAED) pattern of LCAO-25 (as a representative) were collected on samples. The bright field TEM image, shown in **Figure 5.6a**, is also in agreement with the hexagonal morphology of LCAO-25. **Figure 5.6b** shows the high resolution-TEM image of LCAO-25,

with the measured crystal lattice spacing of 4.74 Å that corresponds to the (003) plane. The selected area electron diffraction (SAED) pattern, **(inset of Figure 5.6b)**, exhibits distinct planes that are well indexed with the d-spacing of (003) and (104) crystal planes. This observation reveals that LCAO-25 has a hexagonal structure with a space group of R-3m, which is consistent with the result of Rietveld's refined XRD.

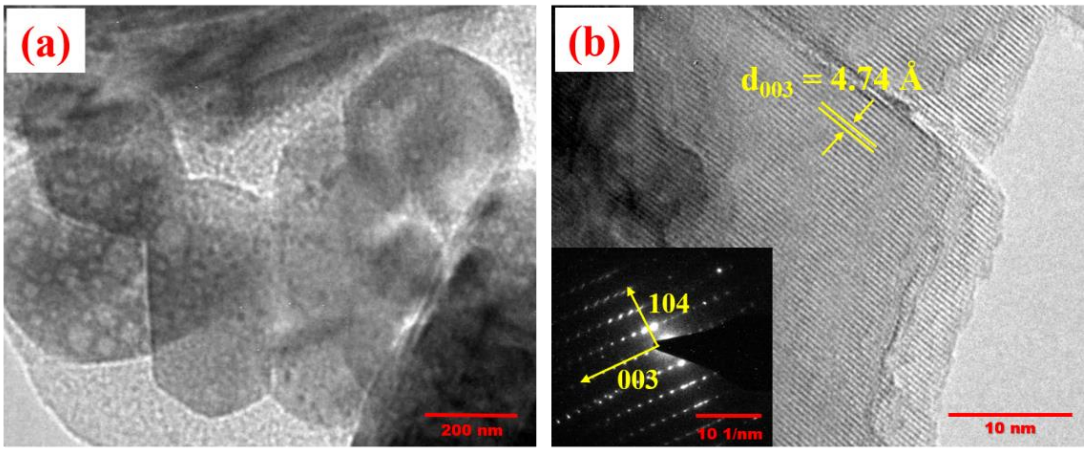

Figure 5.6 (a) Bright field TEM image and **(b)** HR-TEM with interplanar d-spacing of (003) plane of LCAO-25; inset showing the SAED pattern.

5.3.4 Electrochemical studies

5.3.4.1 OER performances of synthesized catalysts

To investigate the electrocatalytic activity of the LCAO catalysts, a traditional three-electrode cell was set up in an O_2-saturated 1.0 M KOH solution to evaluate the OER performance. Several scans of cyclic voltammogram (CV) were performed on the working electrode to obtain a stable current, at a scan rate of 100 mV s^{-1} in the potential range of 1.0–1.8 V vs. RHE, before collecting the data. **Figure 5.7a** shows the linear sweep voltammetry (LSV) curves of all the synthesized LCAO catalysts. It has been observed from the curves that the OER current densities were enhanced with increasing Al concentration to 25% and then reduced upon further increasing the Al concentration beyond 25%. The OER activity increased in the order of LCAO-17 < LCAO-0 < LCAO-20 < LCAO-33 < LCAO-25. Based on 10% solar water-

splitting conversion efficiency, an overpotential (η) required to attain the current density of 10 mA cm^{-2} is indeed a critical metric in the field of solar fuel synthesis, consequently comparing the overpotential of the catalyst samples at this current density is of great importance. The overpotential in this context is defined as the difference between the measured OER potential at 10 mA cm^{-2} and the theoretical reversible potential (1.23 V vs. RHE). LCAO-25 can deliver 10 mA cm^{-2} current density at a very low overpotential of 327 mV, which is significantly lower than 346 mV, 366 mV, 374 mV, and 389 mV for LCAO-33, LCAO-20, LCAO-0, and LCAO-17, respectively, **(Figure 5.7b)**.

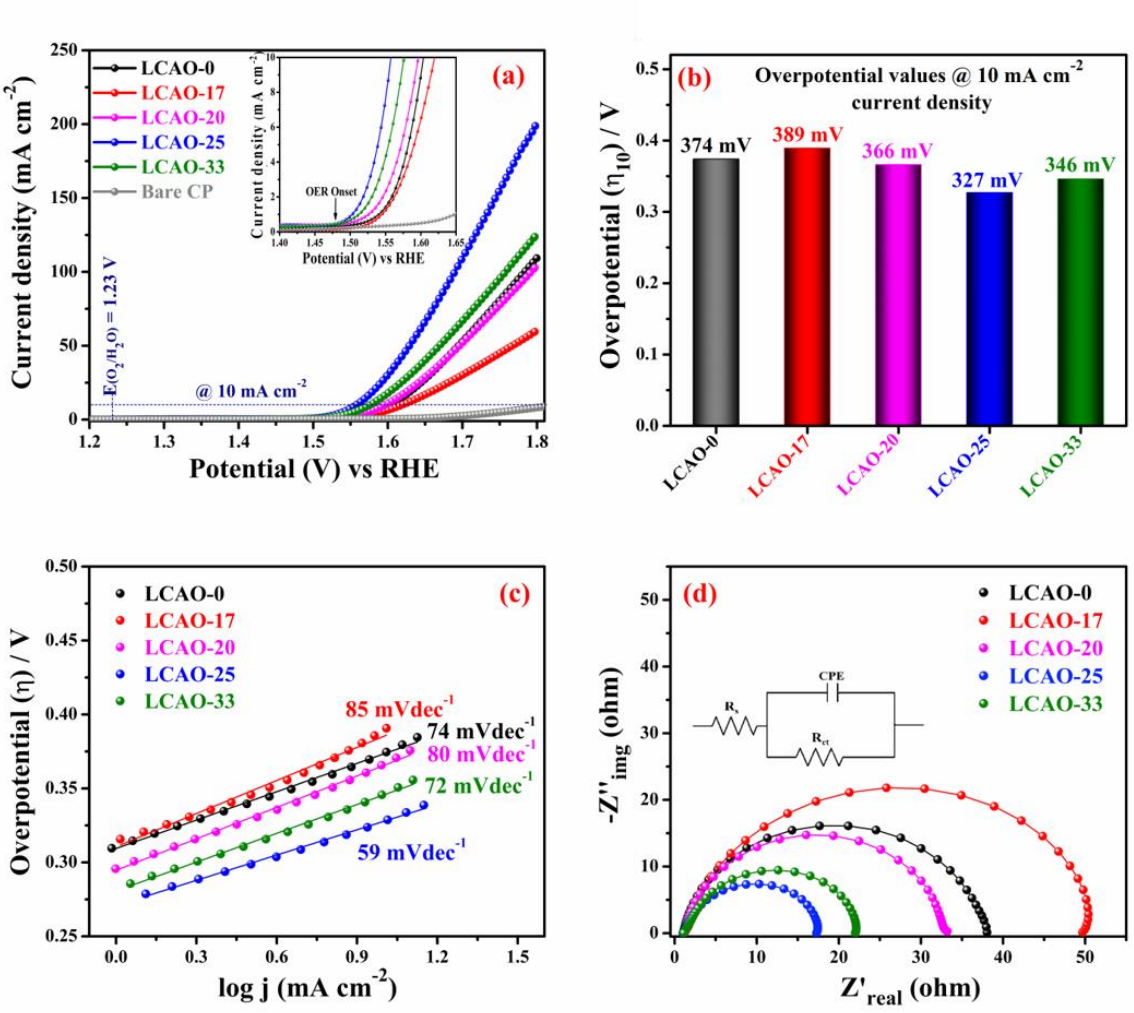

Figure 5.7 OER performance of LCAOs ($Li_{1-x}Cr_{1-x}Al_xO_2$; x = 0, 0.17, 0.20, 0.25, 0.33). **(a)** Linear sweep voltammograms taken at a scan rate of 5 mV s^{-1} in 1 M KOH, **(b)** Overpotentials at a current density of 10 mA cm^{-2}, **(c)** Tafel plots and **(d)** EIS recorded at 1.5 V vs. RHE.

Tafel plots define the relationship between the overpotential to the current density and provide a significant insight into the OER kinetics. The Tafel slopes for all the synthesized LCAOs are drawn in **Figure 5.7c**. The slope value for LCAO-25 is about 59 mV dec^{-1}, which is considerably lower than that of the LCAO-0 (74 mV dec^{-1}), LCAO-17 (85 mV dec^{-1}), LCAO-20 (80 mV dec^{-1}), and LCAO-33 (72 mV dec^{-1}). This clearly implied a faster reaction kinetics of LCAO-25 among all LCAOs. Furthermore, the electrochemical impedance spectroscopy (EIS) measurements were performed to investigate the kinetics of charge transfer at the electrode/electrolyte interface in a frequency region of 0.1 Hz to 100 kHz with 10 mV of AC amplitude. **Figure 5.7d** shows the Nyquist plots at 1.5 V vs. RHE, which can be fitted using an equivalent circuit composed of electrolyte resistance (R_s), a constant phase element (CPE), and a charge transfer resistance (R_{ct}), (**inset of Figure. 5.7d**). The high-frequency region semicircle diameter represents the charge-transfer resistance (R_{ct}), which is a crucial parameter to study the OER kinetics of catalysts. The R_{ct} value can significantly reduce with increasing Al concentration to an optimum value of 25%. The order of the R_{ct} value is: LCAO-25 (16.17 Ω) < LCAO-33 (20.89 Ω) < LCAO-20 (32.09 Ω) < LCAO-0 (37.03 Ω) < LCAO-17 (48.33 Ω). The minimum R_{ct} value was achieved on LCAO-25 (16.17 Ω), which specifies that it shows considerably much faster charge transfer kinetics during the OER process.

5.3.4.2 Electrochemical active surface area (ECSA)

Electrocatalysts with more active sites are known to result in greater catalytic performance. The electrocatalytic activity is directly related to the electrochemically active surface area (ECSA) of the catalysts, which can be determined by measuring the electrochemical double-layer capacitance in the non-faradaic region at different scan rates. The ECSA is directly proportional to the double-layer capacitance (C_{dl}). The ECSA of the catalyst was calculated by using the formula:

$$ECSA = \frac{C_{dl}}{C_s} \quad (5.2)$$

Where C_{dl} is the double-layer capacitance of the catalyst and C_s is the specific capacitance of the material per unit area under identical electrolyte conditions. C_s = 0.040 mF cm^{-2} in 1.0 M KOH based on reported values [9].

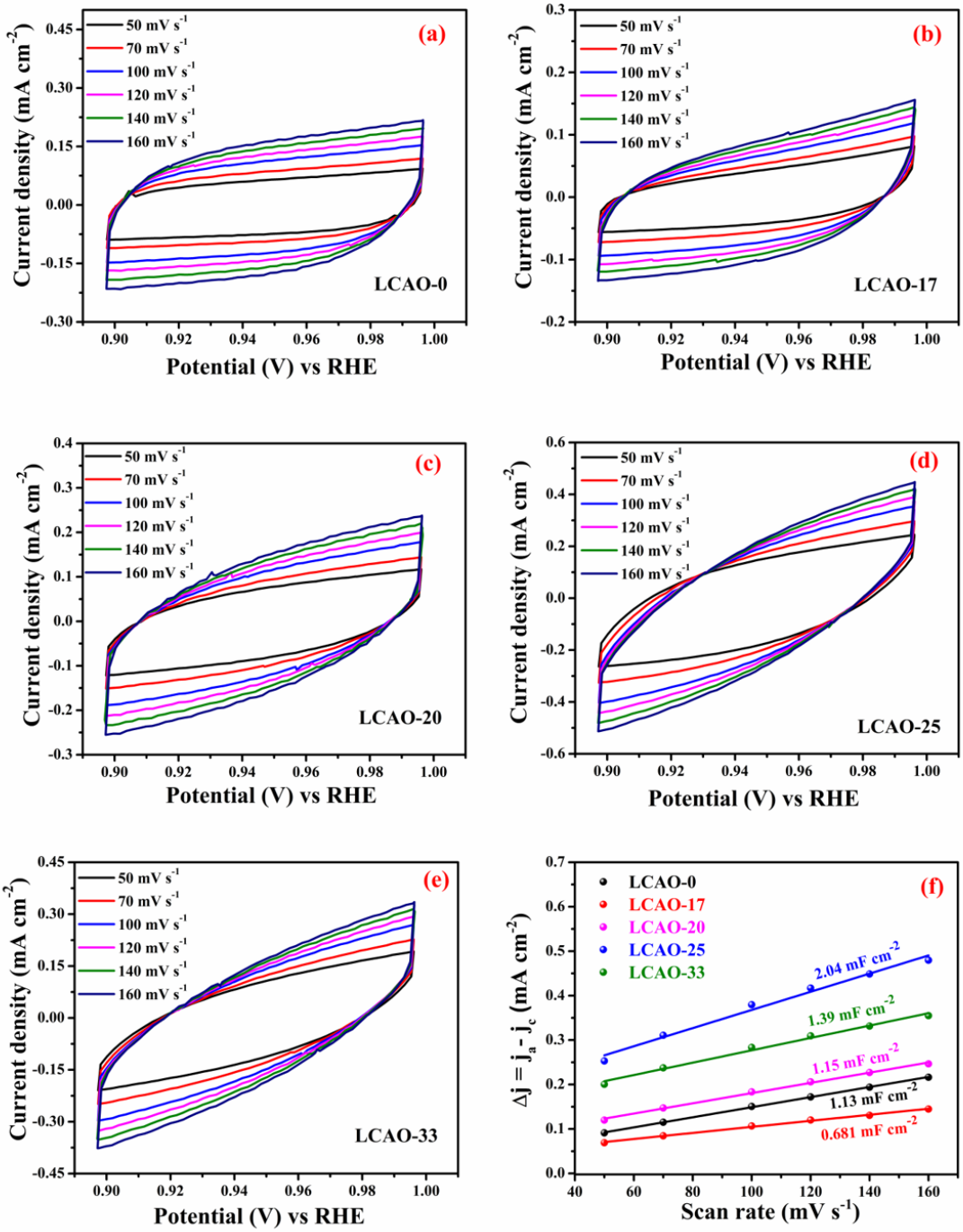

Figure 5.8 Determination of double layer capacitance (C_{dl}) of different LCAOs. **(a-e)** CV measurements in a non-faradic current region (0.9-1.0 V vs. RHE) at scan rates of 50, 100, 120, 140 and 160 mV s^{-1}in 1 M KOH electrolyte and **(f)** Plots of capacitive current density differences (Δj) vs. scan rate.

Here, the double layer capacitance (C_{dl}) of the synthesized catalysts was calculated through cyclic voltammetry measurements in the potential range of 0.9-1.0 V vs. RHE at scan rates of 50, 70, 100, 120, 140, and 160 mV s^{-1}, as shown in **Figure 5.8(a-e)**. As we can see, LCAO-25 exhibits a C_{dl} value (2.04 mF cm^{-2}) and hence the highest ECSA (51 cm^2 mg^{-1}) among all the synthesized LCAO catalysts **(Figure 5.8f & Table 5.3)**. Thus, we concluded that LCAO-25 with higher ECSA makes a larger amount of reactant adsorption for OER.

Table 5.3 Determination of C_{dl} and ECSA of LCAOs.

Catalyst	C_{dl} (mF cm^{-2})	ECSA (cm^2 mg^{-1})
LCAO-0	1.13	28.25
LCAO-17	0.681	17.025
LCAO-20	1.15	28.75
LCAO-25	1.39	34.75
LCAO-33	2.04	51

5.3.4.3 Comparative OER study

A comparison of the OER activity of LCAO-25 with the state-of-the-art catalysts such as commercial-RuO_2 (Sigma-Aldrich), $Ba_{0.5}Sr_{0.5}Co_{0.8}Fe_{0.2}O_{3-\delta}$ (BSCF), $LaNiO_3$, α-MnO_2 in the literature is shown in **Figure 5.9**. In this work, we have tested the OER activities of all the reference catalysts under the same experimental conditions. α-MnO_2 [23], $Ba_{0.5}Sr_{0.5}Co_{0.8}Fe_{0.2}O_{3-\delta}$ (BSCF) [24], $LaNiO_3$ [43, 44], and RuO_2 [22, 45] showed the OER activity similar to the reported in the literature. The activity of LCAO-25 (327 mV at 10 mA cm^{-2}) remarkably approaches the performance of benchmark oxide catalyst RuO_2 (336 mV at 10 mA cm^{-2}) [22, 45], as is evident from **Figure 5.9a**. Further, we have observed that the overpotential value (η_{10} = 327 mV) obtained for LCAO-25 is much smaller as compared to the value obtained for BSCF (η_{10} = 360 mV), $LaNiO_3$ (η_{10} = 380 mV) and α-MnO_2 (η_{10} = 490 mV),

see **Figure 5.9b**. Besides, the Tafel plot and Nyquist plot were also shown in **Figure 5.9(c, d)**, separately. The lower value of the Tafel slope and charge transfer resistance (R_{ct}) of LCAO-25, clearly demonstrates its superior OER activity as compared to these state-of-the-art catalysts.

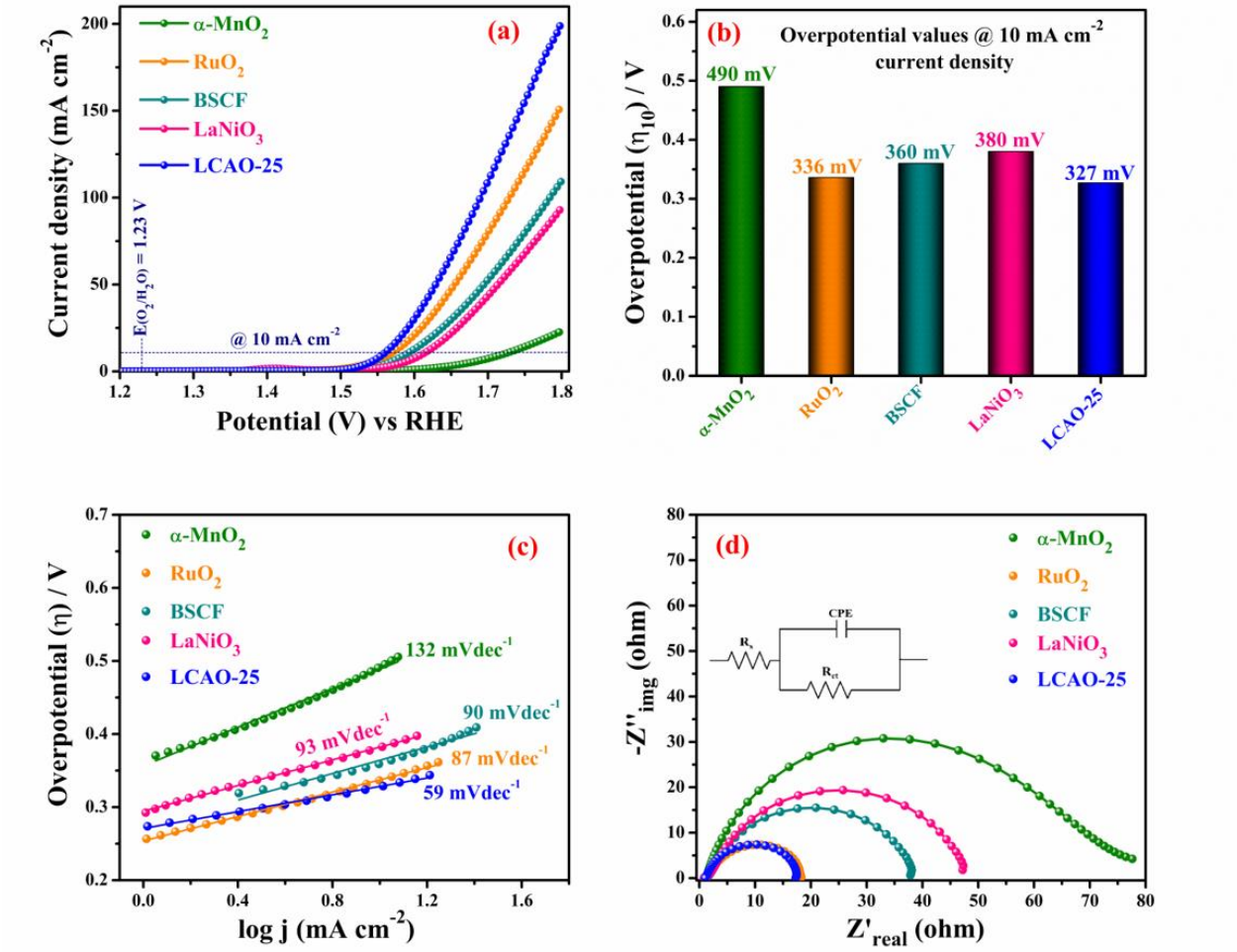

Figure 5.9 Comparison of OER performance of LCAO-25 with commercial RuO_2, α-MnO_2, $Ba_{0.5}Sr_{0.5}Co_{0.8}Fe_{0.2}O_{3-\delta}$ (BSCF), $LaNiO_3$ as reference catalysts; the OER activity of reference catalysts reported in this paper is comparable to the existing literatures [22-24, 43-45]. **(a)** Linear sweep voltammograms recorded at 5 mV s^{-1} in 1 M KOH, **(b)** Overpotentials at a current density of 10 mA cm^{-2}, **(c)** Tafel plots and **(d)** EIS measurement at an applied potential of 1.5 V vs. RHE.

5.3.4.4 Cyclic voltammograms for redox reaction

Previous studies have suggested that the OER activity of metal oxides can be correlated with the potential of redox preceding OER, which also corresponds to the redox of surface metal

ion sites, [M^{n+}-OH_{ad}]/[M^{n+1}-O_{ad}] [11, 13, 16]. The enhanced OER kinetics is accompanied by a positive shift in the redox potential for the oxidation of surface metal ions, before the onset of OER. The pre-OER faradaic behavior of catalysts is presented in **Figure 5.10**, which depicts the in-situ activation of catalysts attributed to the oxidation of Cr^{3+} to Cr^{6+}, a three-electron transfer reaction with single redox [20-22]. All the LCAOs exhibit redox peak potential in the range between 1.3 V-1.5 V vs. RHE. However, the redox potential is found to shift positively with increasing Al concentration in solid solution. This is because of the polarization or inductive effect due to the substitution of highly covalent Al^{3+} ions in the $LiCrO_2$ lattice resulting in high ionicity of the counterpart Cr-O and Li-O bonds in the layered structure.

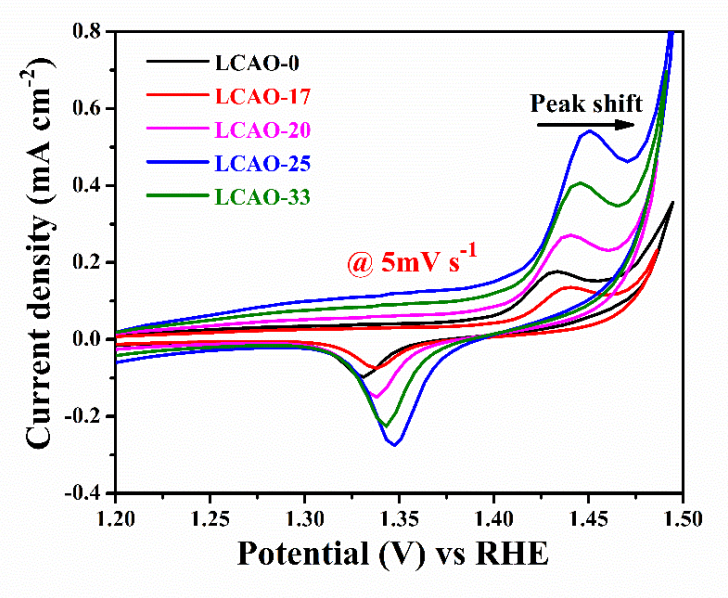

Figure 5.10 Cyclic voltammograms of $Li_{1-x}Cr_{1-x}Al_xO_2$ catalysts with various Al contents (x = 0, 0.17, 0.20, 0.25, 0.33) recorded at a scan rate of 5 mV s^{-1} in 1 M KOH, demonstrating the effect of Al-substitution on the pre-OER redox behaviour of the catalysts.

The more polarizing Al^{3+} ion (with stronger Lewis's acidity) has a higher affinity to electrons than the Cr^{3+} ion, which can induce the formation of more covalent Al-O bond in $Li_{1-x}Cr_{1-x}Al_xO_2$. The high covalency of the Al-O bond can increase the ionicity of neighbouring/counterpart Cr-O and Li-O bonds (by increasing the effective charge on chromium, i.e., Cr^{6+}) that would lead to lowering the redox energy of filled antibonding states,

and shift the redox potential to a more positive side. Moreover, the redox peak center shifts positively with decreasing pK_a (increased Lewis' acidity) of the corresponding substituent (Al) in **Figure 5.10** which is similar to the trends discussed earlier in the literature [11]. As can be seen in the **Figure 5.10**, the redox potential of LCAO-25 shifts more positively among all LCAOs confirming its superior OER activity among all LCAOs.

5.3.4.5 Long-term stability test

Besides the catalytic activity, long-term stability is also required for the practical value of the electrocatalysts. The stability test was performed through cyclic voltammetry (CV), and chronoamperometry (CA) measurements. In **Figure 5.11**, the chronoamperometry (CA) test of LCAO-25 at 1.557 V vs. RHE shows a stable current density of 10 mA cm^{-2} with a negligible loss over 12 h. The inset of **Figure 5.11** presents the LSV curves of LCAO-25 at the 1st, 100th, 500th, and 1000th cycle scans during the continuous cyclic voltammetry (CV) measurements. The slight increase in the potential of the electrocatalyst indicates its good stability even after 1000 CV scans.

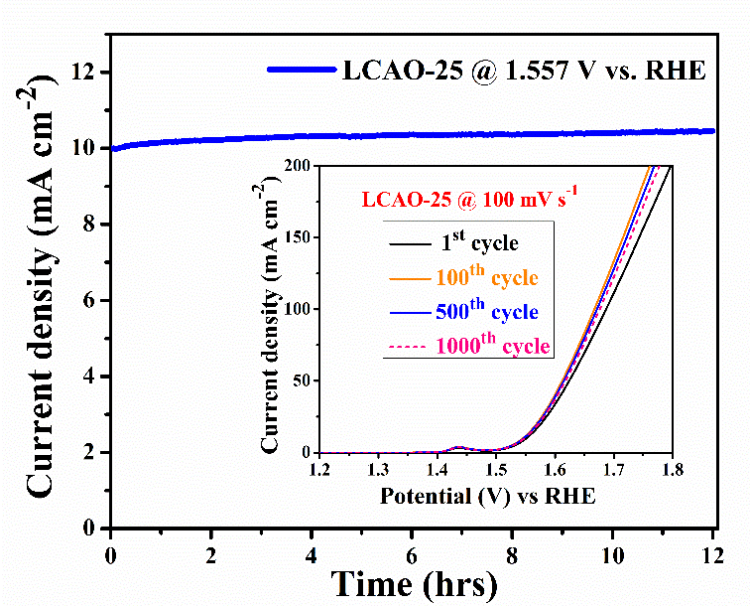

Figure 5.11 Chronoamperogram of LCAO-25 at an applied potential of 1.557 V vs. RHE for 12 hrs; inset shows the linear sweep voltammograms for the 1st, 100th, 500th and 1000th cycle at a scan rate of 100 mV s^{-1}.

5.3.5 Post OER characterizations

The post-OER characterizations of LCAO-25 were carried out to observe any structural changes induced during the electrochemical testing. **Figure 5.12** shows the XRD pattern of the samples (LCAO-25) before and after OER testing. As can be seen, the layered α-$NaFeO_2$ structure is retained even after the long-term stability test. Extra peaks appear in the XRD pattern due to the carbon paper (CP) substrate. No appreciable peak shifting has been observed in the sample after testing. However, the diffraction lines of the post-OER sample are broadened and more diffused compared to the as-prepared sample.

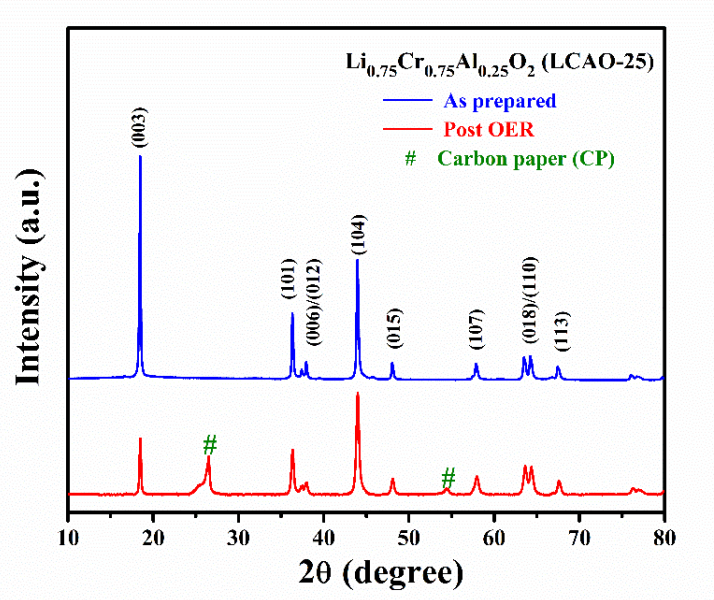

Figure 5.12 XRD pattern of LCAO-25 before and after OER testing.

The pattern shows the relative intensity ratio of the (003) to (104) peak ($I_{(003)}/I_{(104)}$ = 0.6) is notably decreased after OER testing, indicating a significant cation-mixing occurring in the structure during the electrochemical cycling. The structure becomes more Li deficient during the reaction that enables the Cr-ions to move from the Cr-layer into the vacancies of the Li-layer, resulting in a significant cation-mixing. However, the broadening of the diffraction lines indicates that there is a slight decrease in the *c*-axis lattice parameter that would lead to a decrease in the interslab thickness of Li-O layer with increasing the slab thickness of Cr-O

layer due to the presence of Cr-ions in the Li-deficient sites [28, 33]. This can be further confirmed with the XPS analysis of post-OER samples.

Figure 5.13 shows the Cr 2*p* spectra of the as-prepared and post-OER LCAO-25 samples. The respective binding energies of $2p_{3/2}$ and $2p_{1/2}$ peaks corresponding to the Cr^{3+} and Cr^{6+} states with their relative concentration ratios are shown in **Table 5.4** [34, 35]. It is observed that the surface concentration of Cr^{6+} has been increased in the post-OER sample compared to as prepared one. This result clearly confirms the three-electron transfer mechanism of the redox reaction that is attributed to the in-situ oxidation of Cr^{3+} to Cr^{6+} during the electrochemical cycling for OER.

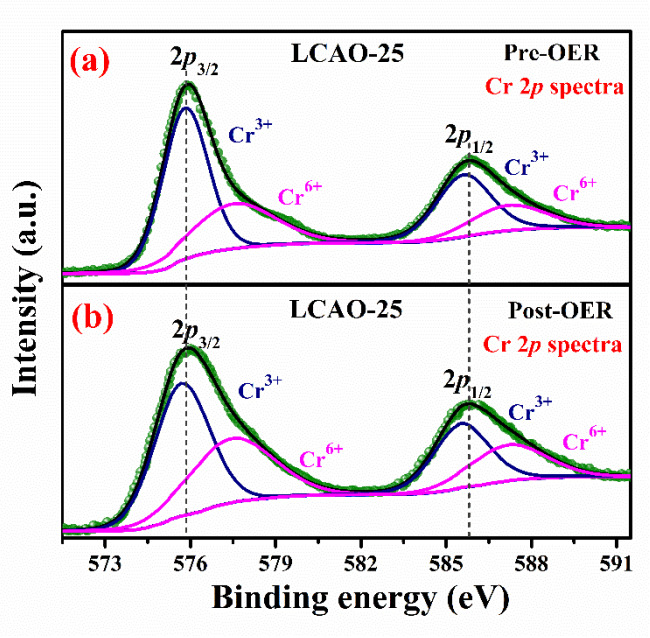

Figure 5.13 Cr 2p XPS spectra of LCAO-25 **(a)** before testing (pre-OER) and **(b)** after testing (post-OER).

Table 5.4 Cr 2p XPS fitting data for pre- and post-OER LCAO-25.

LCAO-25	Binding Energy (eV)				Relative concentration	
	Cr $2p_{3/2}$		Cr $2p_{1/2}$		Cr^{3+}	Cr^{6+}
	Cr^{3+}	Cr^{6+}	Cr^{3+}	Cr^{6+}		
Pre-OER	575.83	577.73	585.69	587.37	0.72	0.28
Post-OER	575.74	577.66	585.56	588.33	0.63	0.37

5.4 Conclusion

$Li_{1-x}Cr_{1-x}Al_xO_2$; x = 0, 0.17, 0.20, 0.25, 0.33) samples having a characteristic hexagonal α-$NaFeO_2$-type structure with the *R-3m* space group were synthesized by solid-state reaction and all diffraction lines are well-indexed with the standard rhombohedral phase of $LiCrO_2$ (JCPDS No. 00-024-0600). The Al/Cr antisites finally stabilize the system in Li-deficient sites. The bonding between the O and Cr/Al present at Li sites shortens the interlayer distance, and the electrostatic attraction between them decreases the total energy of the system. The doping of Al can substantially induce the Cr^{6+} ions to be partially occupied at the Li interstitial site creating a dumbbell defect in the hexagonal lattice of $Li_{1-x}Cr_{1-x}Al_xO_2$ and thereby stabilizing the layered structure of the system with partial Li-deficiency and cation mixing. Al^{3+} substitution in the lattice increases the ionicity of the Cr-O and Li-O bonds in general as well as results in the high concentration of Cr^{6+} ions in the lattice. The more polarizing Al^{3+} ion (with stronger Lewis acidity) have a higher affinity to electrons than the Cr^{3+} ion, that induces the formation of more covalent Al-O bond in $Li_{1-x}Cr_{1-x}Al_xO_2$ and increasing the ionicity of neighbouring/counterpart Cr-O and Li-O bonds (by increasing the effective charge of Cr) which would lead to lowering the redox energy of filled antibonding states, and shift the redox potential to a more positive side to result in superior electrocatalytic OER of the catalyst. The activity of LCAO-25 (327 mV at 10 mA cm^{-2}) remarkably approaches the performance of benchmark oxide catalyst RuO_2 (336 mV at 10 mA cm^{-2}) [22, 45] and showed superior or

comparable OER activity to the best known OER catalyst such as α-MnO_2 [23], $Ba_{0.5}Sr_{0.5}Co_{0.8}Fe_{0.2}O_{3-\delta}$ (BSCF) [24], and $LaNiO_3$ [43, 44]. Our findings suggest that the anisotropic behavior of layered lattice coupled with the tuning of ionicity of M-O bonding in layered oxides can be used as an effective tool in developing superior OER catalysts.

5.5 References

1. Li, J., 2022. Oxygen evolution reaction in energy conversion and storage: design strategies under and beyond the energy scaling relationship. *Nano-Micro Letters*, *14*(1), p.112.
2. Holladay, J.D., Hu, J., King, D.L. and Wang, Y., 2009. An overview of hydrogen production technologies. *Catalysis today*, *139*(4), pp.244-260.
3. Feng, L.L., Yu, G., Wu, Y., Li, G.D., Li, H., Sun, Y., Asefa, T., Chen, W. and Zou, X., 2015. High-index faceted Ni_3S_2 nanosheet arrays as highly active and ultrastable electrocatalysts for water splitting. *Journal of the American Chemical Society*, *137*(44), pp.14023-14026.
4. Jaiswal, S., Mondal, R., Kushwaha, V., Gupta, A. and Singh, P., 2023. Tuning of Redox Energy of Transition-Metal Ions through the Utilization of Interlayer Potentials in Layered Perovskites: Development of a Titanium-Based Superior HER Catalyst in an Acidic Medium. *ACS Applied Energy Materials*, *6*(14), pp.7323-7334.
5. Fabbri, E., Habereder, A., Waltar, K., Kötz, R. and Schmidt, T.J., 2014. Developments and perspectives of oxide-based catalysts for the oxygen evolution reaction. *Catalysis Science & Technology*, *4*(11), pp.3800-3821.
6. Ouyang, T., Ye, Y.Q., Wu, C.Y., Xiao, K. and Liu, Z.Q., 2019. Heterostructures composed of N-doped carbon nanotubes encapsulating cobalt and β-Mo_2C nanoparticles as bifunctional electrodes for water splitting. *Angewandte Chemie International Edition*, *58*(15), pp.4923-4928.
7. Koper, M.T., 2011. Thermodynamic theory of multi-electron transfer reactions: Implications for electrocatalysis. *Journal of Electroanalytical Chemistry*, *660*(2), pp.254-260.
8. Lyons, M.E. and Brandon, M.P., 2010. A comparative study of the oxygen evolution reaction on oxidised nickel, cobalt and iron electrodes in base. *Journal of Electroanalytical Chemistry*, *641*(1-2), pp.119-130.
9. McCrory, C.C., Jung, S., Peters, J.C. and Jaramillo, T.F., 2013. Benchmarking heterogeneous electrocatalysts for the oxygen evolution reaction. *Journal of the American Chemical Society*, *135*(45), pp.16977-16987.
10. Hong, W.T., Risch, M., Stoerzinger, K.A., Grimaud, A., Suntivich, J. and Shao-Horn, Y., 2015. Toward the rational design of non-precious transition metal oxides for oxygen electrocatalysis. *Energy & Environmental Science*, *8*(5), pp.1404-1427.

11. Kuznetsov, D.A., Han, B., Yu, Y., Rao, R.R., Hwang, J., Román-Leshkov, Y. and Shao-Horn, Y., 2018. Tuning redox transitions via inductive effect in metal oxides and complexes, and implications in oxygen electrocatalysis. *Joule*, *2*(2), pp.225-244.
12. Lee, S.W., Carlton, C., Risch, M., Surendranath, Y., Chen, S., Furutsuki, S., Yamada, A., Nocera, D.G. and Shao-Horn, Y., 2012. The nature of lithium battery materials under oxygen evolution reaction conditions. *Journal of the American Chemical Society*, *134*(41), pp.16959-16962.
13. Augustyn, V. and Manthiram, A., 2015. Characterization of Layered $LiMO_2$ Oxides for the Oxygen Evolution Reaction of Metal–Air Batteries (M= Mn, Co, Ni). *ChemPlusChem*, *80*(2), pp.422-427.
14. Lu, Z., Wang, H., Kong, D., Yan, K., Hsu, P.C., Zheng, G., Yao, H., Liang, Z., Sun, X. and Cui, Y., 2014. Electrochemical tuning of layered lithium transition metal oxides for improvement of oxygen evolution reaction. *Nature communications*, *5*(1), p.4345.
15. Maiyalagan, T., Jarvis, K.A., Therese, S., Ferreira, P.J. and Manthiram, A., 2014. Spinel-type lithium cobalt oxide as a bifunctional electrocatalyst for the oxygen evolution and oxygen reduction reactions. *Nature communications*, *5*(1), p.3949.
16. Augustyn, V., Therese, S., Turner, T.C. and Manthiram, A., 2015. Nickel-rich layered $LiNi_{1-x}M_xO_2$ (M= Mn, Fe, and Co) electrocatalysts with high oxygen evolution reaction activity. *Journal of Materials Chemistry A*, *3*(32), pp.16604-16612.
17. Gupta, A., Chemelewski, W.D., Buddie Mullins, C. and Goodenough, J.B., 2015. High-rate oxygen evolution reaction on Al-doped $LiNiO_2$. *Advanced Materials*, *27*(39), pp.6063-6067.
18. Zhu, K., Wu, T., Zhu, Y., Li, X., Li, M., Lu, R., Wang, J., Zhu, X. and Yang, W., 2017. Layered Fe-substituted $LiNiO_2$ electrocatalysts for high-efficiency oxygen evolution reaction. *ACS Energy Letters*, *2*(7), pp.1654-1660.
19. Balasubramanian, M., McBreen, J., Davidson, I.J., Whitfield, P.S. and Kargina, I., 2002. In situ X-ray absorption study of a layered manganese-chromium oxide-based cathode material. *Journal of the electrochemical Society*, *149*(2), p.A176.
20. Lu, Z. and Dahn, J.R., 2002. Structure and electrochemistry of layered $Li[Cr_xLi_{(1/3-x/3)}Mn_{(2/3-2x/3)}]O_2$. *Journal of the Electrochemical Society*, *149*(11), p.A1454.
21. Soni, V., Mondal, R., Singh, A.N., Singh, P. and Gupta, A., 2023. Dumbbell Defect Containing Chromium-Rich Lithium-Vacant Layered $Li_yCr_{1-x}Fe_xO_2$ ($y \leq 1$, $0 \leq x \leq 0.2$): An Unexplored and Highly Efficient Electrocatalyst for the Oxygen Evolution Reaction. *ACS Applied Energy Materials*, *6*(3), pp.1308-1320.

22. Dixit, M., Markovsky, B., Aurbach, D. and Major, D.T., 2017. Unraveling the effects of Al doping on the electrochemical properties of $LiNi_{0.5}Co_{0.2}Mn_{0.3}O_2$ using first principles. *Journal of The Electrochemical Society*, *164*(1), p.A6359.
23. Bera, K., Karmakar, A., Karthick, K., Sankar, S.S., Kumaravel, S., Madhu, R. and Kundu, S., 2021. Enhancement of the OER kinetics of the less-explored α-MnO_2 via nickel doping approaches in alkaline medium. *Inorganic Chemistry*, *60*(24), pp.19429-19439.
24. Tang, L., Zhang, W., Lin, D., Ren, Y., Zheng, H., Luo, Q., Wei, L., Liu, H., Chen, J. and Tang, K., 2020. The hexagonal perovskite $Ba_{0.5}Sr_{0.5}Co_{0.8}Fe_{0.2}O_{3-\delta}$ as an efficient electrocatalyst for the oxygen evolution reaction. *Inorganic Chemistry Frontiers*, *7*(22), pp.4488-4497.
25. Fernandes, J.D., Melo, D.M.D.A., Zinner, L.B., Salustiano, C.D.M., Silva, Z.R., Martinelli, A.E., Cerqueira, M., Junior, C.A., Longo, E. and Bernardi, M.I.B., 2002. Low-temperature synthesis of single-phase crystalline $LaNiO_3$ perovskite via Pechini method. *Materials Letters*, *53*(1-2), pp.122-125.
26. García, S.C., Couceiro, A.C., Rodriguez, M.A.S., Soulette, F. and Julien, C., 2003. Influence of aluminum doping on the properties of $LiCoO_2$ and $LiNi_{0.5}Co_{0.5}O_2$ oxides. *Solid State Ionics*, *156*, p.15.
27. Ohzuku, T., Ueda, A., Nagayama, M., Iwakoshi, Y. and Komori, H., 1993. Comparative study of $LiCoO_2$, $LiNi_{12}Co_{12}O_2$ and $LiNiO_2$ for 4 volt secondary lithium cells. *Electrochimica Acta*, *38*(9), pp.1159-1167.
28. Guilmard, M., Rougier, A., Grüne, M., Croguennec, L. and Delmas, C., 2003. Effects of aluminum on the structural and electrochemical properties of $LiNiO_2$. *Journal of Power Sources*, *115*(2), pp.305-314.
29. File, P.D., 1967. Joint committee on powder diffraction standards. *ASTM, Philadelphia, Pa*, pp.9-185.
30. Vegard, L.; Dale, H.; Krystallogr. Z. 1928, 67, 148.
31. West, A. R. 1984, Solid State Chemistry and its Applications, *Wiley, New York* p. 367.
32. Shannon, R. D. 1976, *Actu Crystallogr. Sect. A*, 32, 751.
33. Lyu, Y., Ben, L., Sun, Y., Tang, D., Xu, K., Gu, L., Xiao, R., Li, H., Chen, L. and Huang, X., 2015. Atomic insight into electrochemical inactivity of lithium chromate ($LiCrO_2$): Irreversible migration of chromium into lithium layers in surface regions. *Journal of Power Sources*, *273*, pp.1218-1225.

34. Feng, G.X., Li, L.F., Liu, J.Y., Liu, N., Li, H., Yang, X.Q., Huang, X.J., Chen, L.Q., Nam, K.W. and Yoon, W.S., 2009. Enhanced electrochemical lithium storage activity of $LiCrO_2$ by size effect. *Journal of Materials Chemistry*, *19*(19), pp.2993-2998.
35. Singh, P., Hegde, M.S. and Gopalakrishnan, J., 2008. $Ce_{2/3}Cr_{1/3}O_{2+y}$: a new oxygen storage material based on the fluorite structure. *Chemistry of Materials*, *20*(23), pp.7268-7273.
36. Xiao, B., Tang, Q., Dai, X., Wu, F., Chen, H., Li, J., Mai, Y. and Gu, Y., 2022. Enhanced Interfacial Kinetics and High Rate Performance of $LiCoO_2$ Thin-Film Electrodes by Al Doping and In Situ Al_2O_3 Coating. *ACS omega*, *7*(35), pp.31597-31606.
37. Andreeva, R.A., Stoyanova, E.A., Tsanev, A.S. and Stoychev, D.S., 2016. Corrosion behavior of anodically formed oxide films on aluminum, sealed in cerium-ions containing solutions. *Bulg. Chem. Commun*, *48*, pp.96-102.
38. Limcharoen, A., Pakpum, C. and Limsuwan, P., 2012. An X-ray photoelectron spectroscopy investigation of redeposition from fluorine-based plasma etch on magnetic recording slider head substrate. *Procedia Engineering*, *32*, pp.1043-1049.
39. Cherkashinin, G., Nikolowski, K., Ehrenberg, H., Jacke, S., Dimesso, L. and Jaegermann, W., 2012. The stability of the SEI layer, surface composition and the oxidation state of transition metals at the electrolyte–cathode interface impacted by the electrochemical cycling: X-ray photoelectron spectroscopy investigation. *Physical Chemistry Chemical Physics*, *14*(35), pp.12321-12331.
40. Gupta, A., Kumar, A., Waghmare, U.V. and Hegde, M.S., 2009. Origin of activation of lattice oxygen and synergistic interaction in bimetal-ionic $Ce_{0.89}Fe_{0.1}Pd_{0.01}O_{2-\delta}$ catalyst. *Chemistry of materials*, *21*(20), pp.4880-4891.
41. Scofield, J.H., 1976. Hartree-Slater subshell photoionization cross-sections at 1254 and 1487 eV. *Journal of Electron Spectroscopy and Related Phenomena*, *8*(2), pp.129-137.
42. Penn, D.R., 1976. Quantitative chemical analysis by ESCA. *Journal of Electron Spectroscopy and Related Phenomena*, *9*(1), pp.29-40.
43. Petrie, J.R., Cooper, V.R., Freeland, J.W., Meyer, T.L., Zhang, Z., Lutterman, D.A. and Lee, H.N., 2016. Enhanced bifunctional oxygen catalysis in strained $LaNiO_3$ perovskites. *Journal of the American Chemical Society*, *138*(8), pp.2488-2491.
44. Chen, J., Wu, J., Liu, Y., Hu, X. and Geng, D., 2018. Assemblage of Perovskite $LaNiO_3$ Connected with In Situ Grown Nitrogen-Doped Carbon Nanotubes as High-Performance Electrocatalyst for Oxygen Evolution Reaction. *physica status solidi (a)*, *215*(21), p.1800380.

45. Anantharaj, S., Reddy, P.N. and Kundu, S., 2017. Core-oxidized amorphous cobalt phosphide nanostructures: an advanced and highly efficient oxygen evolution catalyst. *Inorganic Chemistry*, *56*(3), pp.1742-1756.